Energy Advances

ROYAL SOCIETY OF CHEMISTRY

PAPER

View Article Online
View Journal | View Issue

Cite this: *Energy Adv.*, 2025, 4, 896

Oxygen vacancy assisted hydrogen evolution reaction over CeO_2-based solid solutions

Saraswati Roy [a] and Sounak Roy *[ab]

Received 2nd February 2025,
Accepted 18th May 2025

DOI: 10.1039/d5ya00027k

rsc.li/energy-advances

Producing sustainable hydrogen through water electrolysis is a promising approach to meet the growing demand for renewable energy storage. Developing affordable and efficient electrocatalysts made from non-precious metals to replace platinum-based catalysts for hydrogen evolution reactions (HERs) continues to be a significant challenge. In the present study, pristine CeO_2 and doped solid solutions $Ce_{0.95}Co_{0.05}O_2$, $Ce_{0.95}Ni_{0.05}O_2$ and $Ce_{0.95}Cu_{0.05}O_2$ were evaluated for the HER, and the electrochemical studies in alkaline medium showed superior HER activity for the doped catalysts, with $Ce_{0.95}Ni_{0.05}O_2$ achieving the lowest overpotential and highest mass activity, comparable to Pt/C. Tafel slopes and EIS measurements suggested a Volmer–Heyrovsky mechanism facilitated by oxygen vacancies and hydrogen spill-over. Stability tests confirmed the durability of $Ce_{0.95}Ni_{0.05}O_2$ under prolonged HER conditions. This study highlights aliovalent doping as a viable strategy for engineering oxygen vacancies and enhancing CeO_2-based catalysts for alkaline water electrolysis.

1. Introduction

The continued reliance on fossil fuels not only depletes these finite resources but also contributes to a host of environmental problems. Hydrogen stands out as a clean and efficient energy carrier, representing a significant step forward in building a hydrogen-driven economy. However, it's important to recognize that although using hydrogen fuel does not directly produce CO_2 emissions, many current methods of hydrogen production do contribute to CO_2 emissions. In this regard, water electrolysis with the help of renewable electricity has significant potential to produce affordable, sustainable green hydrogen on a large scale. After its first discovery in 1789, the HER has been one of the most extensively studied processes in electrocatalysis, primarily owing to its straightforward mechanism involving two consecutive proton–electron transfers without side reactions.[1–5] Although Pt group metals and their alloys are some of the most efficient electrocatalysts for the HER, reducing costs is essential to make water electrolysis a practical method for H_2 production. To achieve this, extensive research is currently directed toward developing affordable, stable, and efficient HER catalysts using non-noble metals.[6–11]

Conventional alkaline electrolyzers typically rely on electrodes made from late transition metals like Co, Ni, and Cu because of their affordability and outstanding chemical durability.[12,13] Oxides of Co, Ni, and Cu are considered promising catalysts for the HER due to their low energy barriers for hydrogen adsorption.[14–16] However, a significant challenge associated with these cathodes is their low conductivity, which hinders efficient electron transfer during the HER process. One common approach to enhancing conductivity is to introduce highly conductive substrates,[17–20] while another method is to create oxygen vacancies.[21–23] Enhanced oxygen vacancy concentrations in electrocatalysts can be achieved by introducing highly reducible oxides as a support for the transition metal active sites. The distinctive ability to reversibly switch between Ce^{3+} and Ce^{4+} oxidation states, combined with the presence of abundant oxygen vacancy defects and surface oxygen ion exchange renders CeO_2 a promising support material, capable of forming an active metal–support interface with significant electrochemical activity.[24,25] For example, in a recent study, Ni-based composites over commercial CeO_2 nanoparticles exhibited a 48% higher current density compared to the conventional Ni-Watts catalyst. The authors attributed this improvement to the interaction between the Fermi level of Ni and CeO_2, which induced band bending and modulated the electrocatalytic activity toward H_2 generation. In another study, 2% Gd doped CeO_2 in 1.0 M KOH showed HER with an overpotential of 99 mV and a Tafel slope of 211 mv dec^{-1}.[26] Similarly, Ni-doped CeO_2 supported on N-doped carbon nanofibers (Ni/CeO_2@N-CNFs) exhibited an overpotential of 100 mV and a Tafel slope of 85.7 mV dec^{-1} in 1.0 M KOH alkaline electrolyte.[27] Ni–S alloys on the surface of CeO_2 nanorods and CeO_2 nano flex demonstrated HER overpotential of 200 and 180 mV at a current density of 10 mA cm^{-2} in 1.0 M NaOH.[28]

[a] *Department of Chemistry, Birla Institute of Technology and Science Pilani, Hyderabad Campus, Hyderabad 500078, India.*
E-mail: sounak.roy@hyderabad.bits-pilani.ac.in
[b] *Materials Center for Sustainable Energy & Environment, Birla Institute of Technology and Science Pilani, Hyderabad Campus, Hyderabad 500078, India*

In another investigation, Ni/MoO_{2-x}@NF showed a HER overpotential of 27 mV with a Tafel slope of 26 mv dec^{-1} in 1.0 M KOH.[29,30] Furthermore, Ce-doped Ni_2P, with a Ce/Ni atomic ratio of 12.3%, showed overpotentials of 77 mV and 42 mV to achieve a current density of 10 mA cm^{-2} in 1 M KOH and 0.5 M H_2SO_4 solutions, respectively.[31] Notably, in most of the reports, the supported metal catalysts consist of the active metal or metal oxide dispersed on the surface of CeO_2.

We have recently carried out a series of studies with CeO_2 as a promising support to the transition metal active site due to its easily available redox of Ce^{4+}/Ce^{3+}, which is responsible for oxygen vacancy enhancement.[32–34] In our studies, the active metal sites (M^{n+}) were ionically substituted in the fluorite CeO_2 matrix to produce a solid solution of $Ce_{1-x}M_xO_2$. The aliovalent doping of ionic active sites enhanced reducibility and generated oxygen vacancies in CeO_2. We have demonstrated that the formation of the solid solution of $Ce_{1-x}M_xO_2$ immensely facilitated the reduction of $Ce^{4+} \rightarrow Ce^{3+}$ and subsequent oxidation of $M^{n+} \rightarrow M^{(n+1)+}$ during anodic oxidation reactions. However, in our previous investigations, the focus was primarily on anodic oxidation reactions. In this study, for the first time, we have evaluated the performances of pristine CeO_2, and doped solid solutions of $Ce_{0.95}Co_{0.05}O_2$, $Ce_{0.95}Ni_{0.05}O_2$ and $Ce_{0.95}Cu_{0.05}O_2$ in the HER. The primary focus is to investigate the role of support reducibility and oxygen vacancies in influencing HER kinetics. This study developed a novel, cost-effective, and efficient material for the HER, and also came up with a meaningful insight into the fundamental mechanisms.

2. Materials and methods

2.1. Synthesis and characterization of CeO_2, $Ce_{0.95}Co_{0.05}O_2$, $Ce_{0.95}Ni_{0.05}O_2$ and $Ce_{0.95}Cu_{0.05}O_2$

The pristine and the doped materials were synthesized using the solution combustion method. The solution combustion method is advantageous as it is a low temperature initiated single step self-propagating process with a high transient temperature producing huge amounts of gases. The combustion process is fast (instantaneous) and due to the production of huge amounts of gases, the products are homogenous nanocrystalline materials with the desired composition and structure. This process utilizes the highly exothermic redox chemical reactions between metal nitrates and fuels. The details of the synthesis of CeO_2, $Ce_{0.95}Co_{0.05}O_2$, $Ce_{0.95}Ni_{0.05}O_2$ and $Ce_{0.95}Cu_{0.05}O_2$ are provided in our previous study.[32]

The structure and crystallinity of the synthesized mixed metal oxides were analysed through X-ray diffraction (XRD) using a Rigaku Ultima IV instrument equipped with Cu Kα radiation. The XRD scans were conducted at a scanning rate of 0.4° per minute, with a step size of 0.01°. The surface morphology and compositional analysis were performed using a field emission scanning electron microscope (FESEM) integrated with energy dispersive X-ray spectroscopy (EDS). An acceleration voltage of 20 kV was used to run the device. An Al Kα radiation (1486.6 eV) Thermo Scientific K-Alpha surface analysis spectrometer was used to capture the synthesised catalysts' X-ray photoelectron spectra (XPS). A nonlinear least-squares curve fitting program with a Gaussian–Lorentzian production function was applied to the data profiles, and Avantage software was used for processing. The standard C 1s peak at 284.85 eV was used to calibrate the binding energy (B.E.) of all XPS data. The absorption and steady-state photoluminescence (PL) spectra were recorded using a Fluoro-Log spectrofluorimeter (Horiba Scientific) and a JASCO UV-Vis spectrophotometer (model no. V-650). A Bruker ESR 5000 was used to perform the EPR study. Raman spectroscopy was performed using UniRam Raman spectroscopy.

2.2. Electrochemical studies

A standard three-electrode system was used to perform electrochemical testing on the synthesised compounds. A synthesised catalyst was applied to carbon cloth to create the working electrode. Pt mesh was employed as the counter electrode, while the reference electrode was Hg/HgO saturated with an aqueous KOH solution. 3 mg of the synthesised catalyst and 0.5 mg of powdered carbon black were mixed with one ml of methanol to create the working electrode. Furthermore, the solution was supplemented with 10 μl of 5% aqueous Nafion (Sigma-Aldrich). To produce a uniform dispersion of the carbon and the synthesised metal oxides, the mixture was sonicated for 60 minutes. At 6 : 1.5, the catalyst's active mass ratio to carbon black was kept constant. After chopping into 1 × 0.4 cm^2 pieces, the carbon cloth electrode was agitated in 3 : 1 HNO_3 and H_2SO_4 for three hours at 80 °C. It was then cleaned with distilled water and agitated in distilled water for four hours at 80 °C. The produced ink comprising 50 μl of the catalyst was drop-cast onto the clean carbon cloth electrode with an active mass loading of 0.15 mg cm^{-2} after the carbon cloth had been dried for the entire night. At room temperature, the electrode was allowed to dry. Overall, electrocatalytic water splitting was performed using an Origa Flex OGF500 electrochemical workstation. Electrochemical impedance spectroscopy (EIS), linear sweep voltammetry (LSV), and cyclic voltammetry (CV) were measured at a scan rate of 10 mV s^{-1} in a simple electrolyte medium of 1 M KOH. Between 0 and −0.6 V (*versus* RHE), the CV cycles and the HER polarization curves were performed using LSV traces. The following formula was used to convert the acquired potentials to the reversible hydrogen electrode (RHE): $E_{RHE} = E_{Hg/HgO} + 0.059\ pH + E^0_{Hg/HgO}$. In this case, $E_{Hg/HgO}$ is the experimental potential with regard to the Hg/HgO electrode, $E^0_{Hg/HgO}$ is the standard reduction potential of the Hg/HgO electrode, and E_{RHE} is the final converted potential with regard to RHE. For the water splitting reaction, a two-electrode arrangement was chosen. Chronoamperometric (CA) measurements were carried out in a three-electrode system for 24 hours in 1 M KOH in order to assess material stability. EIS was performed using overpotential *vs.* Hg/HgO in the frequency range of 100 kHz to 10 mHz. A portable gas chromatograph (GC) from Mayura Analytical Pvt. Limited in India was used to measure the gaseous product H_2.

3. Results and discussion

3.1. Structure and oxygen vacancies

The single-step solution combustion approach produced nanocrystalline and porous pure CeO_2 and the solid solutions $Ce_{0.95}Co_{0.05}O_2$, $Ce_{0.95}Ni_{0.05}O_2$, and $Ce_{0.95}Cu_{0.05}O_2$ with uniform dopant distribution.[35–38] The development of the nano-sized porous particles is confirmed by the FE-SEM micrographs of pristine CeO_2 and the doped solid solutions $Ce_{0.95}Co_{0.05}O_2$, $Ce_{0.95}Ni_{0.05}O_2$, and $Ce_{0.95}Cu_{0.05}O_2$ shown in Fig. 1. The particle size distribution was within around 100 nm. A constant doping concentration with the theoretically computed values was validated by the elemental atomic percentages obtained from EDX examination.

All of the synthesized materials' powder XRD patterns are shown in Fig. 2(a). The materials crystallized in a phase-pure cubic fluorite structure with the space group $Fm\bar{3}m$. No extra diffraction peaks corresponding to secondary phases like Co_3O_4, NiO, or CuO were observed in the doped oxides $Ce_{0.95}Co_{0.05}O_2$, $Ce_{0.95}Ni_{0.05}O_2$, and $Ce_{0.95}Cu_{0.05}O_2$. This absence of extraneous peaks confirms the successful formation of phase-pure solid solutions. The synthesized materials displayed relatively broad diffraction peaks, indicative of their nanocrystalline nature, which is attributed to the specific characteristics of the solution

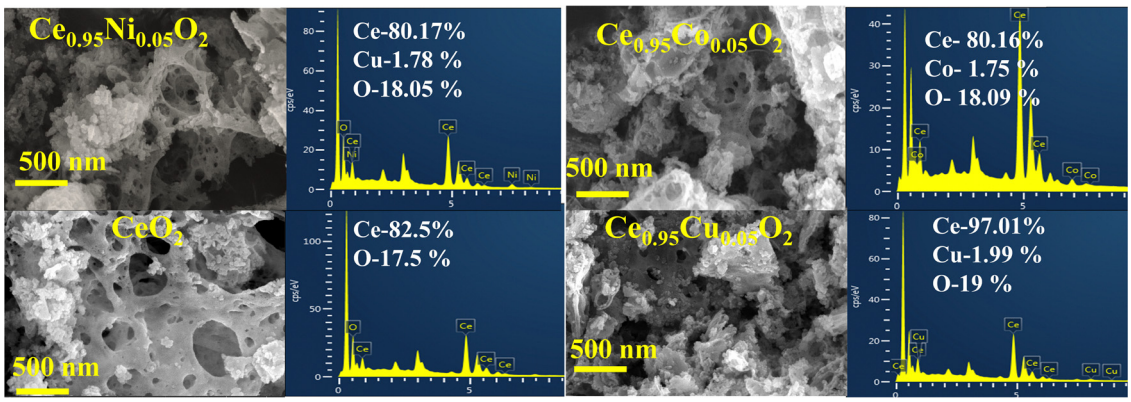

Fig. 1 FE-SEM and EDX of CeO_2 and doped $Ce_{0.95}Co_{0.05}O_2$, $Ce_{0.95}Ni_{0.05}O_2$, and $Ce_{0.95}Cu_{0.05}O_2$.

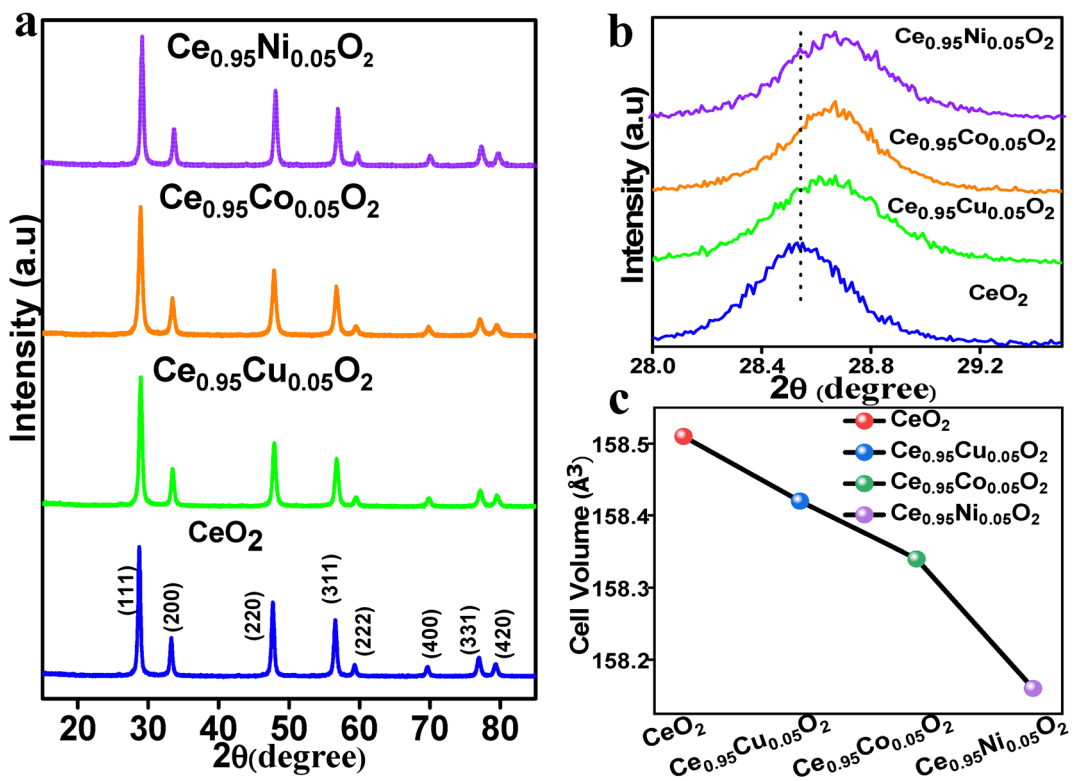

Fig. 2 (a) XRD patterns, (b) zoomed in version, (c) the refined cell volume of CeO_2 and doped $Ce_{0.95}Co_{0.05}O_2$, $Ce_{0.95}Ni_{0.05}O_2$, and $Ce_{0.95}Cu_{0.05}O_2$.

combustion synthesis. Interestingly, upon doping in CeO_2, a noticeable shift of the diffraction peaks towards higher angles was observed (Fig. 2(b)), indicating a reduction in the unit cell volume. The Shannon ionic radius of eight-coordinated Ce^{4+} in the fluorite lattice is 0.97 Å, whereas the ionic radii of divalent Co, Ni, and Cu range from 0.65 to 0.75 Å. The diffraction peaks may shift to higher angles and the unit cell volume may decrease when Ce^{4+} is substituted with smaller cations like Co^{2+}, Ni^{2+}, and Cu^{2+}. The experimentally obtained diffraction patterns were subjected to Rietveld refinement in order to validate these structural alterations. During the refinement, Co, Ni, and Cu cations were modelled at the 4a Wyckoff sites typically occupied by Ce. Details are provided elsewhere.[32] The cell volumes derived from the refinement, plotted in Fig. 2(c), further confirm the unit cell contraction, corroborating the formation of substitutional solid solutions.

We subsequently looked at the surface characteristics of the produced materials. In the N_2 adsorption–desorption isotherms, both the pristine and doped solid solutions displayed a type II isotherm with a small hysteresis, indicating the surface's nanoporous nature. The average specific surface area, as determined by the BET equation, was around 20 $m^2\ g^{-1}$ (Fig. 3(a)). Fig. 3(b) and (c) show the non-faradaic region CV and C_{dl} plots, respectively. The typical ECSA values were calculated from the observed C_{dl} values. Fig. 3(d) shows the 3-fold increased ECSA of $Ce_{0.95}Ni_{0.05}O_2$ compared to pristine CeO_2.

Doping with aliovalent substitution would cause extrinsic oxygen vacancies to emerge in the CeO_2 matrix. O 1s core-level XPS data were collected in order to conduct a detailed analysis of the oxygen vacancies (Fig. 4(a)). In the O 1s XPS spectra, the peak at 529.2 eV corresponds to lattice oxygen (O_L), while the peak at 531.7 eV is attributed to adsorbed oxygen species associated with surface defect sites, particularly oxygen vacancies (O_V). CeO_2, $Ce_{0.95}Cu_{0.05}O_2$, $Ce_{0.95}Co_{0.05}O_2$, and $Ce_{0.95}Ni_{0.05}O_2$ were found to have surface oxygen vacancy concentrations of 10%, 17%, 38%, and 57%, respectively. The highest concentration of surface oxygen vacancies was observed in $Ce_{0.95}Ni_{0.05}O_2$. Under 310 nm excitation, PL investigations were conducted to further evaluate the existence of oxygen vacancies. Fig. 4(b) depicts the highest intensity of the PL spectrum for pristine CeO_2. The radiative

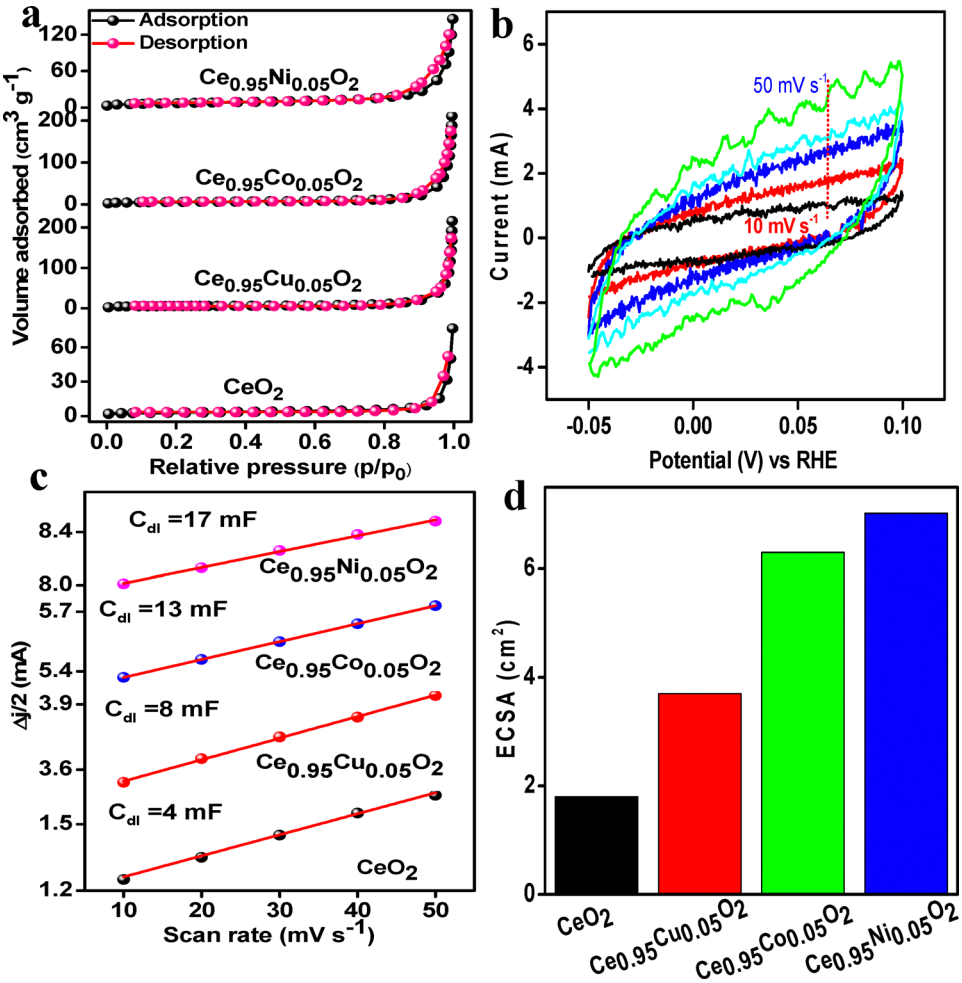

Fig. 3 (a) N_2 adsorption–desorption isotherms of the synthesized catalysts; (b) CV curves of $Ce_{0.95}Ni_{0.05}O_2$ in the non-faradaic region (−0.05 to 0.1 V *vs.* RHE) at scan rates of 10, 20, 30, 40, 50 mV s^{-1}; (c) linear regression between the current density differences in the 0.02 V potential window of CV *vs.* scan rate and (d) ECSA of all four catalysts.

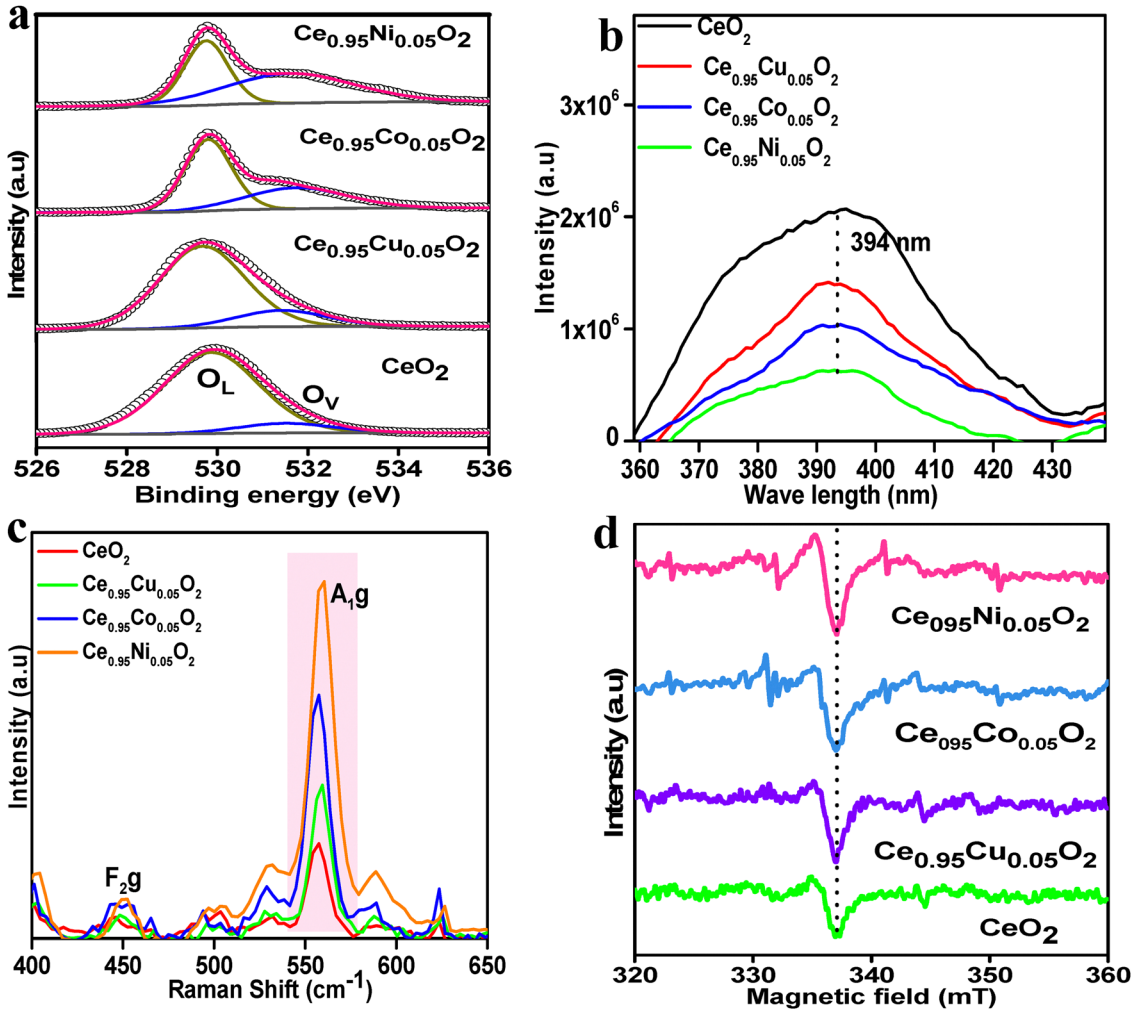

Fig. 4 (a) O1s core level XPS spectra; (b) PL; (c) Raman and (d) EPR spectra of CeO_2 and doped $Ce_{0.95}Co_{0.05}O_2$, $Ce_{0.95}Ni_{0.05}O_2$ and $Ce_{0.95}Cu_{0.05}O_2$.

recombination of holes trapped in reduced Ce^{4+} states with electrons located in intrinsic oxygen vacancies (F-centres) produces the strong PL emission band seen in pristine CeO_2.[39,40] Upon doping, a notable reduction in PL intensity was observed, with $Ce_{0.95}Ni_{0.05}O_2$ exhibiting the lowest intensity. The extrinsic oxygen vacancies generated due to the aliovalent doping can form intermediate electronic states within the bandgap.[41] These states may facilitate non-radiative recombination pathways, thereby suppressing radiative electron–hole recombination and reducing PL intensity. The PL studies verified that the doped solid solutions have more oxygen vacancies than pure CeO_2, with $Ce_{0.95}Ni_{0.05}O_2$ having the highest concentration of oxygen vacancies. Additionally, Raman spectroscopy was used to verify that oxygen vacancies were present. Fig. 4(c) shows a Gaussian peak at around 558 cm^{-1} attributed to the A_{1g} mode, which is suggestive of oxygen vacancies, and a distinctive Lorentzian peak at about 448 cm^{-1}, which corresponds to the F_{2g} vibrational mode of the CeO_2 lattice.[42] The largest oxygen vacancy concentration in $Ce_{0.95}Ni_{0.05}O_2$ was further supported by the maximum intensity of the A_{1g} mode over $Ce_{0.95}Ni_{0.05}O_2$. To look into the existence of oxygen vacancies further, EPR measurements were also carried out. In agreement with the signal ascribed to unpaired electrons close to oxygen vacancies, the *g*-value was found to be approximately 2. The peak intensity at about 336 mT systematically increased with doping, as seen in Fig. 4(d). This enhancement in intensity is attributed to the presence of surface oxygen vacancies.[43] Electrons originally localized in the O 2p orbitals adjacent to these vacancies become delocalized, contributing to the observed EPR signal. Comprehensive analyses using XPS, PL, Raman, and EPR conclusively demonstrated an enhancement in oxygen vacancies resulting from substitutional doping, with $Ce_{0.95}Ni_{0.05}O_2$ exhibiting the highest concentration of oxygen vacancies.

3.2. HER

LSV polarization curves in a 1.0 M KOH solution utilizing a three-electrode setup operating between 0 and −0.6 V (*vs.* RHE) were used to assess the cathodic HER activity of the produced materials. The alkaline electrolyte was chosen herein as alkaline water electrolysis is a highly significant technology that is widely used in the industry, especially for controlling alkaline effluents from processes like water–alkali and chlor–alkali

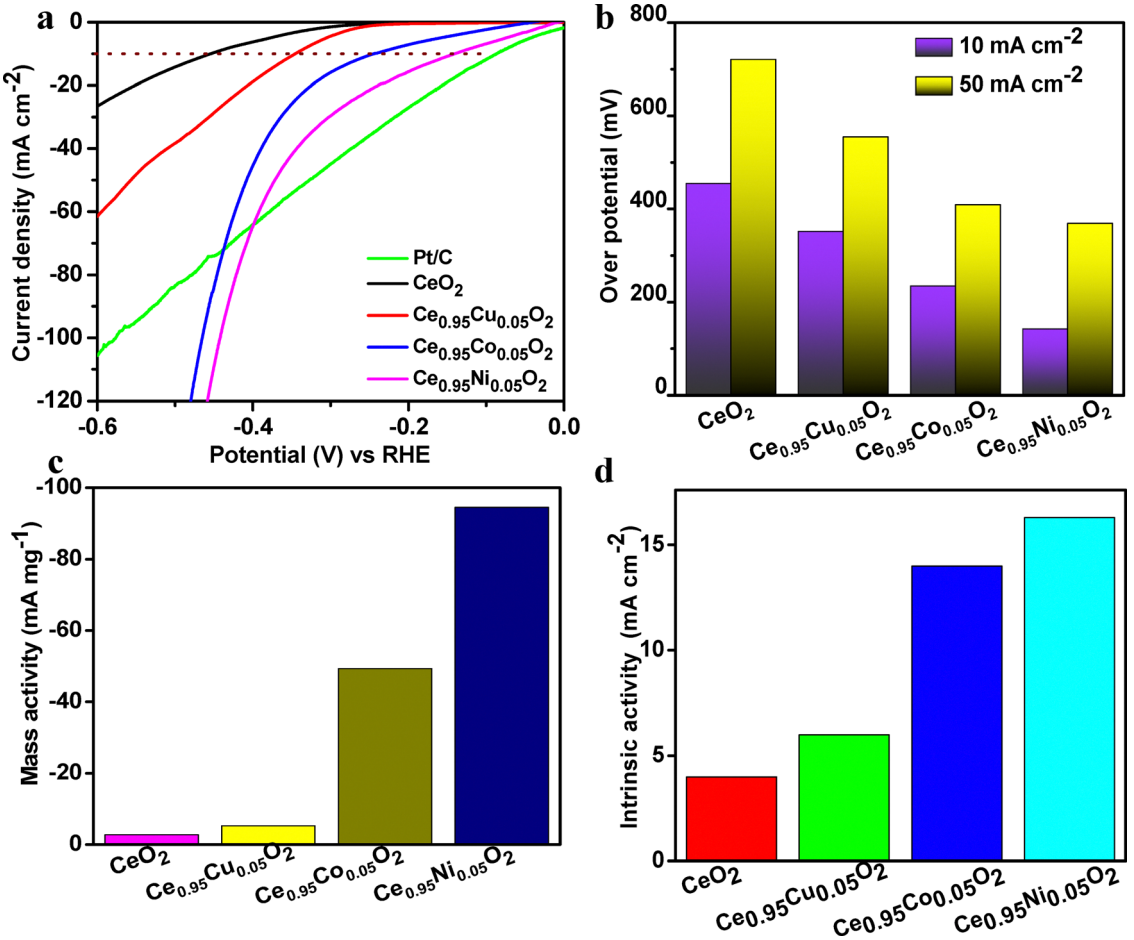

Fig. 5 (a) HER polarisation curve of the synthesized four catalysts with commercial Pt/C; (b) overpotentials; (c) intrinsic mass activity of the synthesized catalysts, and (d) intrinsic activity of the synthesized catalyst.

electrolyzers.[44] As illustrated in Fig. 5(a), the solid solution catalysts demonstrated significantly higher HER activity compared to pristine CeO_2, with $Ce_{0.95}Ni_{0.05}O_2$ exhibiting the lowest overpotential among all synthesized catalysts. A commercial 5% Pt/C sample was also examined under the same circumstances as the benchmark. Only a limited number of HER electrocatalysts have been reported with commercial Pt/C in alkaline electrolyte in the literature compared to that of acidic medium. The overpotential of $Ce_{0.95}Ni_{0.05}O_2$ was remarkably close to that of 5% Pt/C. The required overpotential to reach a current density of 10 mA cm^{-2} is a commonly accepted benchmark standard for the production of solar fuel. The overpotentials for the synthesized materials at current densities of 10 and 50 mA cm^{-2} are shown in Fig. 5(b). The catalysts mass activity derived by normalizing the current density to the amount of catalyst was also ascertained to aid in global comparisons (Fig. 5(c)). The overpotentials as well as the mass activity data show that $Ce_{0.95}Ni_{0.05}O_2$ as a significantly better catalyst than the pure and other doped oxides. Intrinsic activity was also determined for the catalysts (Fig. 5(d)). Intrinsic activity assessments help identify catalysts capable of delivering high current densities, which is critical for efficient and scalable hydrogen production.[45] The intrinsic activity analysis revealed that $Ce_{0.95}Ni_{0.05}O_2$ exhibits superior reactivity compared to the other catalysts studied (Fig. 5(d)).

The electrochemical stability of the most active catalyst, $Ce_{0.95}Ni_{0.05}O_2$ was assessed *via* chronoamperometry in 1.0 M KOH for 48 hours at its corresponding HER overpotential and −0.25 V. As shown in Fig. 6(a), the catalyst maintained a remarkably stable current density. A stepwise CA experiment was conducted over 30 hours using six different potentials, each applied for a 5-hour interval (Fig. 6(b)). The results in Fig. 6(b) demonstrate that the $Ce_{0.95}Ni_{0.05}O_2$ catalyst remains highly stable under both low and high applied potentials. The study reveals a sharp change in the HER potential upon switching the current density, indicating efficient charge and mass transport facilitated by effective electrolyte diffusion within the porous and vertically aligned electrode structure. Furthermore, the electrodes maintain a dimensionally stable architecture, which is advantageous for sustained high-rate hydrogen production.[46]

The superior HER performance of $Ce_{0.95}Ni_{0.05}O_2$ was further validated by the amount of H_2 evolved during the reaction, measured using gas chromatography. Representative chromatograms

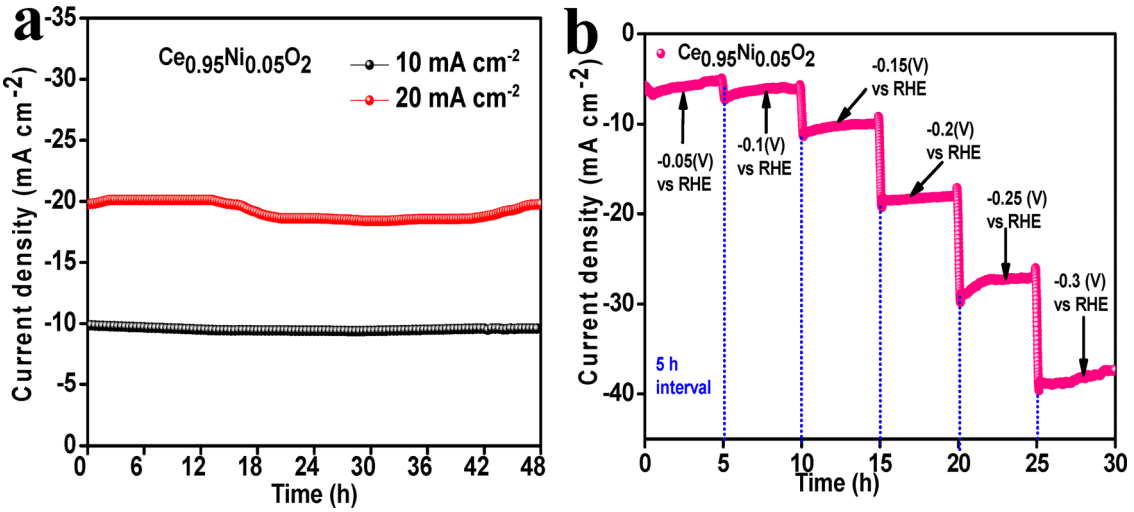

Fig. 6 (a) Stability studies with $Ce_{0.95}Ni_{0.05}O_2$ at 10 and 20 mA cm^{-2} and (b) stepwise CA study of $Ce_{0.95}Ni_{0.05}O_2$.

over $Ce_{0.95}Ni_{0.05}O_2$ in different potentials are provided in Fig. 7(a). The faradaic efficiency for H_2 evolution (FE_{H_2}%) was calculated and is presented in Fig. 7(b). Notably, $Ce_{0.95}Ni_{0.05}O_2$ exhibited an impressive FE_{H_2}% of approximately 88%, surpassing the values obtained for the other pristine and doped catalysts. This high faradaic efficiency indicates that a significant proportion of the electrons supplied during the reaction were effectively utilized for hydrogen production, highlighting the material's exceptional selectivity and efficiency for the HER. The relationship of HER activity on scan rate and activation energy was thoroughly assessed in order to clarify the kinetics of the HER for the produced catalysts. The scan rate dependency tests were carried out by altering the scan rate from 10 to 50 mV s^{-1} in the presence of 1.0 M KOH electrolyte. The CV at different scan rates of $Ce_{0.95}Ni_{0.05}O_2$ are shown in Fig. 7(c). A diffusion-controlled electrocatalytic process on the catalysts was suggested as the HER current density increased linearly with the square root of the scan rate in Fig. 7(d). The activation energy was calculated using an Arrhenius plot of current density ($\ln j$) *vs.* temperature (T^{-1}) at the HER potential of the four catalysts. The LSV traces of $Ce_{0.95}Ni_{0.05}O_2$ at different temperatures are shown in Fig. 7(e). Fig. 7(f) shows the activation energy of different catalysts. While Cu, Co, and Ni doped CeO_2 showed activation energies of 12.97, 10.26, and 9.27 kJ mol^{-1}, respectively, pristine CeO_2 had an activation energy of 13.36 kJ mol^{-1}. The fastest HER kinetics over $Ce_{0.95}Ni_{0.05}O_{2-\delta}$ were indicated by the lowest activation energy.

3.3. Mechanism and surface–reactivity relationship

It is well-established that water electrolysis follows different mechanisms depending on the electrolyte. For instance, the abundance of protons in acidic electrolytes facilitates HER catalysis, whereas achieving the HER at low overpotentials is comparatively more challenging in alkaline media.[47] In alkaline solutions, additional energy is required to generate protons through water molecule dissociation, which subsequently affects the overall reaction rate. The evolution of electrocatalytic hydrogen in alkaline medium is a multi-step process. The Volmer step is the initial step in an alkaline medium (eqn (1)):

$$H_2O + e^- \rightarrow H^* + OH^- \quad (1)$$

Subsequent to this step, the HER pathway in alkaline medium follows the Volmer–Heyrovsky path (eqn (2)) or Volmer–Tafel path (eqn (3)) to produce H_2.

$$H_2O + e^- + H^* \rightarrow H_2 + HO^- \quad (2)$$

$$H^* + H^* \rightarrow H_2 \quad (3)$$

All the above listed reaction phenomenon strongly depend on the inherent surface chemistry leading to charge transfer capabilities of the catalyst. The charge transfer capabilities *vis à vis* Tafel slopes determined from the LSV curves reveal the catalytic kinetics information of the HER. For the HER, a theoretical Tafel slope of 120 mV dec^{-1} corresponds to the Volmer step, whereas 40 and 30 mV dec^{-1} represent the Volmer–Heyrovsky path and Volmer–Tafel path, respectively.[48] Therefore, the Tafel slopes were calculated over the combustion synthesized solid solutions along with the commercial Pt/C catalyst (Fig. 8(a)). It is conventionally believed that Pt-based electrocatalysts go through the Volmer–Tafel path at least in low-potential regions because of the optimal Gibbs free energy of Pt–H* ($\Delta G_{H^*} = 0$).[22] The calculated Tafel slope in our experimental conditions over commercial Pt/C was found to be 35.6 mV dec^{-1} indicating the Volmer–Tafel path in accordance with the literature. However, the Tafel slope calculated over doped $Ce_{0.95}Ni_{0.05}O_2$ was 48 mV dec^{-1} suggesting the Volmer–Heyrovsky mechanistic path of the HER. $Ce_{0.95}Ni_{0.05}O_2$ showed the lowest Tafel slope among the doped solid solutions, and it was reduced by 28% compared with that of pristine CeO_2. An effective electrocatalyst with significant charge transfer capabilities should exhibit a low Tafel slope. Ni in $Ce_{0.95}Ni_{0.05}O_2$ is believed to initially adsorb the H* effectively. The substantial presence of oxygen vacancies in $Ce_{0.95}Ni_{0.05}O_2$, as established from the detailed spectroscopic studies, facilitates the migration of H* from the Ni site to the

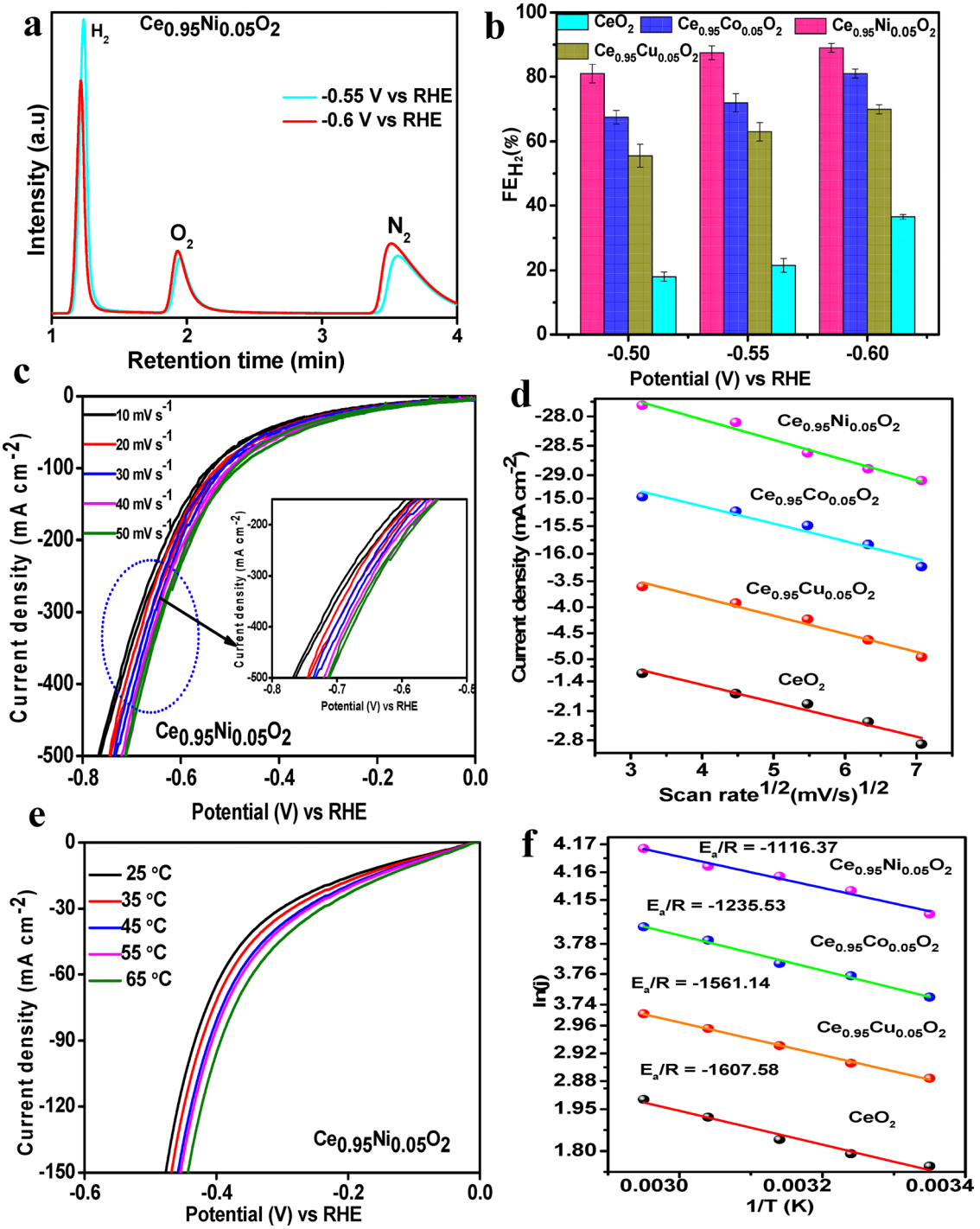

Fig. 7 (a) Representative GC chromatograms of H_2 from $Ce_{0.95}Ni_{0.05}O_2$ after 1 h of chronoamperometric study; (b) FE_{H_2}% of the four catalysts at varied potentials; (c) CV of $Ce_{0.95}Ni_{0.05}O_2$ with different scan rates; (d) scan rate-dependent study of the four catalysts; (e) LSV of $Ce_{0.95}Ni_{0.05}O_2$ at various temperatures and (f) activation energy plot of the hydrogen evolution reaction over the four synthesized materials.

neighbouring vacancy, a well-known hydrogen spill-over phenomenon (eqn (4)).[49] The spilled over H* reacts through the Volmer–Heyrovsky mechanistic path with another water molecule in reducing cathodic potential to produce H_2 (eqn (5)).

$$Ce_{0.95}Ni_{0.05}O_2\square_\delta + \delta H^* \rightarrow Ce_{0.95}Ni_{0.05}O_2\boxed{H}_\delta \quad (4)$$

$$H_2O + e^- + Ce_{0.95}Ni_{0.05}O_2\boxed{H}_\delta \rightarrow H_2 + HO^- + Ce_{0.95}Ni_{0.05}O_2\square_\delta \quad (5)$$

The Tafel slopes obtained for the other synthesized catalysts suggest that this specific mechanistic pathway occurs more sluggishly over other solid-solution catalysts in comparison to

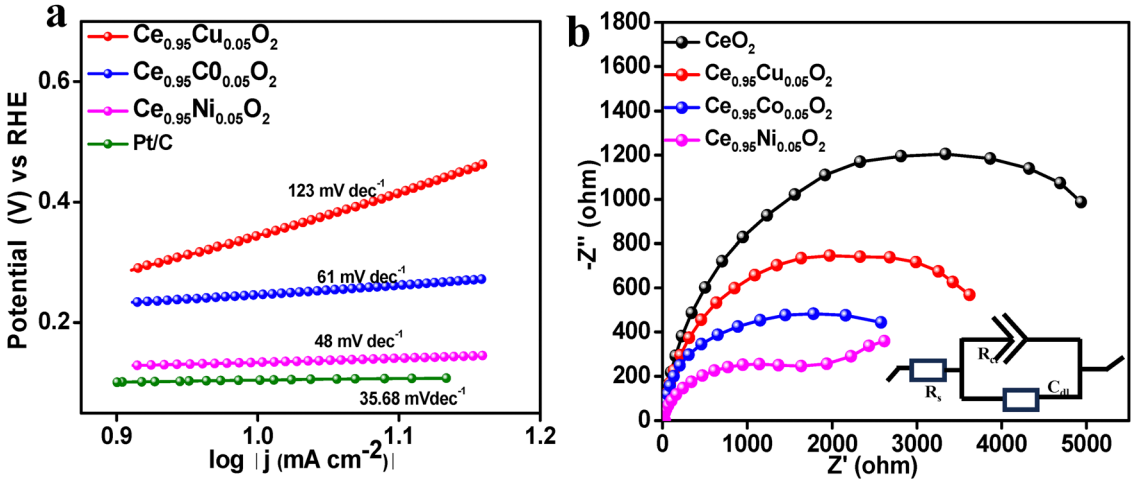

Fig. 8 (a) Tafel plots and (b) EIS studies of the synthesized catalysts.

$Ce_{0.95}Ni_{0.05}O_2$. The highest Tafel slope observed for CeO_2 indicates the slowest HER kinetics for the pristine material. The reduced Tafel slope over $Ce_{0.95}Ni_{0.05}O_2$ also signifies the enhanced charge transfer between the electrode and electrolyte. Therefore, the EIS studies were conducted under the HER conditions and the data are shown in Fig. 8(b). The fitted circuit is provided in the inset of Fig. 8(b). $Ce_{0.95}Ni_{0.05}O_2$ showed the lowest semi-circle suggesting the fastest shuttling of charges corroborating the superiority of the material. The significant presence of oxygen vacancies in $Ce_{0.95}Ni_{0.05}O_2$ likely accounts for its low charge transfer resistance. The R_{ct} values were found to be 4.9×10^3, 3.6×10^3, 2.5×10^3 and 1.3×10^3 Ω for CeO_2, $Ce_{0.95}Cu_{0.05}O_2$, $Ce_{0.95}Co_{0.05}O_2$ and $Ce_{0.95}Ni_{0.05}O_2$, respectively.

The above Volmer–Heyrovsky mechanistic path mediated through the oxygen vacancy assisted H spill-over phenomenon should result in reduction of active sites of ionically doped transition metals as well as the support CeO_2. Therefore, a thorough XPS study was conducted to probe the surface elemental composition and oxidation states of the freshly prepared and exhausted catalysts. Fig. 9(a) represents the Ce 3d core level deconvoluted spectra ($3d_{5/2}$ is labelled as v, and $3d_{3/2}$ is labelled as u) from the as-synthesized catalysts. The spectra exhibited a total of 5 spin orbit coupled peaks, in which v–u, v″–u″, and v‴–u‴ belong to Ce^{4+}, and v^0–u^0 and v′–u′ belong to Ce^{3+}. The Ce^{4+} doublets designated as v–u (882.6–901.3 eV), v″–u″ (889.2–907.6 eV) and v‴–u‴ (897.6–917.0 eV) are associated with Ce $3d^94f^2O2p^4$, Ce $3d^94f^1O2p^5$ and Ce $3d^94f^0O2p^6$ final states, respectively.[50–52] The other two doublets of Ce^{3+} positioned at v^0–u^0 (880–898.5 eV) and v′–u′ (885.4–903.5) correspond to the Ce $3d^94f^2O2p^5$ and Ce $3d^94f^1O2p^6$ final states. The deconvoluted Ce 3d spectra indicated the coexistence of Ce in both the 4+ and 3+ oxidation states in all four as-prepared catalysts. The amount of Ce^{4+} present in CeO_2 and doped $Ce_{0.95}Cu_{0.05}O_2$, $Ce_{0.95}Co_{0.05}O_2$ and $Ce_{0.95}Ni_{0.05}O_2$ was 88, 80, 70 and 66%, respectively. The Cu 2p core level spectra of $Ce_{0.95}Cu_{0.05}O_2$ in Fig. 9(b) show the deconvoluted Cu $2p_{3/2}$ and Cu $2p_{1/2}$ peaks associated with Cu^{2+} as well as Cu^{1+} ions. Peaks at 935.7–955.1 eV appeared for Cu^{2+} $2p_{3/2}$–$2p_{1/2}$ and peaks at 933.7–953.4 eV appeared for Cu^{1+} $2p_{3/2}$–$2p_{1/2}$.[32,53–55] The amount of Cu^{1+} was found to be 76% in the as-prepared $Ce_{0.95}Cu_{0.05}O_2$.[56] Similarly, Fig. 9(c) shows the Co 2p core level deconvoluted spectrum of $Ce_{0.95}Co_{0.05}O_2$. Peaks at 781.8–796.2 eV appeared for Co^{2+} $2p_{3/2}$–$2p_{1/2}$ and peaks at 779.7–794.5 eV were attributed to Co^{3+} $2p_{3/2}$–$2p_{1/2}$.[57–59] The amount of Co^{2+} was found to be 67% in the as-prepared $Ce_{0.95}Cu_{0.05}O_2$. Furthermore, the Ni 2p core level spectrum investigated for $Ce_{0.95}Ni_{0.05}O_2$ in Fig. 9(d) shows the Ni $2p_{3/2}$ and $2p_{1/2}$ peaks associated with Ni^{2+} as well as Ni^{3+} ions. The Ni^{3+} peak appeared at higher binding energy ($2p_{3/2}$–$2p_{1/2}$ at 856.7–874 eV) compared to Ni^{2+} ($2p_{3/2}$–$2p_{1/2}$ at 855–872.8 eV).[60,61] The amount of Ni^{2+} was found to be 68% in the as-prepared $Ce_{0.95}Ni_{0.05}O_2$. It is noteworthy that the doped transition metal ions in the synthesized oxides predominantly exhibited lower-valent oxidation states.

XRD analysis was performed on the spent $Ce_{0.95}Ni_{0.05}O_2$ catalyst (Fig. 10(a)), revealing that the crystal structure remained stable even after long-term stability testing. The absence of any additional peaks in the post-reaction XRD pattern confirmed that no structural changes had occurred. FE-SEM (inset, Fig. 10(a)) and EDX (Fig. 10(b)) analyses showed minor agglomeration of particles following the reaction.

The core-level deconvoluted XPS spectrum of Ce 3d for the four exhausted catalysts is presented in Fig. 11(a). The spectra displayed five spin–orbit coupled peaks, attributed to the Ce^{4+} and Ce^{3+} oxidation states, which agreed with those observed in the fresh catalysts. Fig. 11(a) illustrates the characteristic change of v^0 peak from the fresh catalysts. Following the HER, the concentration of Ce^{4+} in the exhausted catalyst was reduced to 77, 66, 56 and 45% for CeO_2, $Ce_{0.95}Cu_{0.05}O_2$, $Ce_{0.95}Co_{0.05}O_2$, and $Ce_{0.95}Ni_{0.05}O_2$, respectively. The reduction of the formal charge of Ce^{4+} supports the H spill-over phenomenon from the metal to the support. Furthermore, we have conducted the core level XPS of Cu, Co and Ni from exhausted catalysts $Ce_{0.95}Cu_{0.05}O_2$ (Fig. 11(b)), $Ce_{0.95}Co_{0.05}O_2$ (Fig. 11(c)), and $Ce_{0.95}Ni_{0.05}O_2$ (Fig. 11(d)). Cu and Co were found in their reduced oxidation states after the HER. The Ni 2p spectra for the exhausted $Ce_{0.95}Ni_{0.05}O_2$, shown in Fig. 11(d), reveal that 73% of

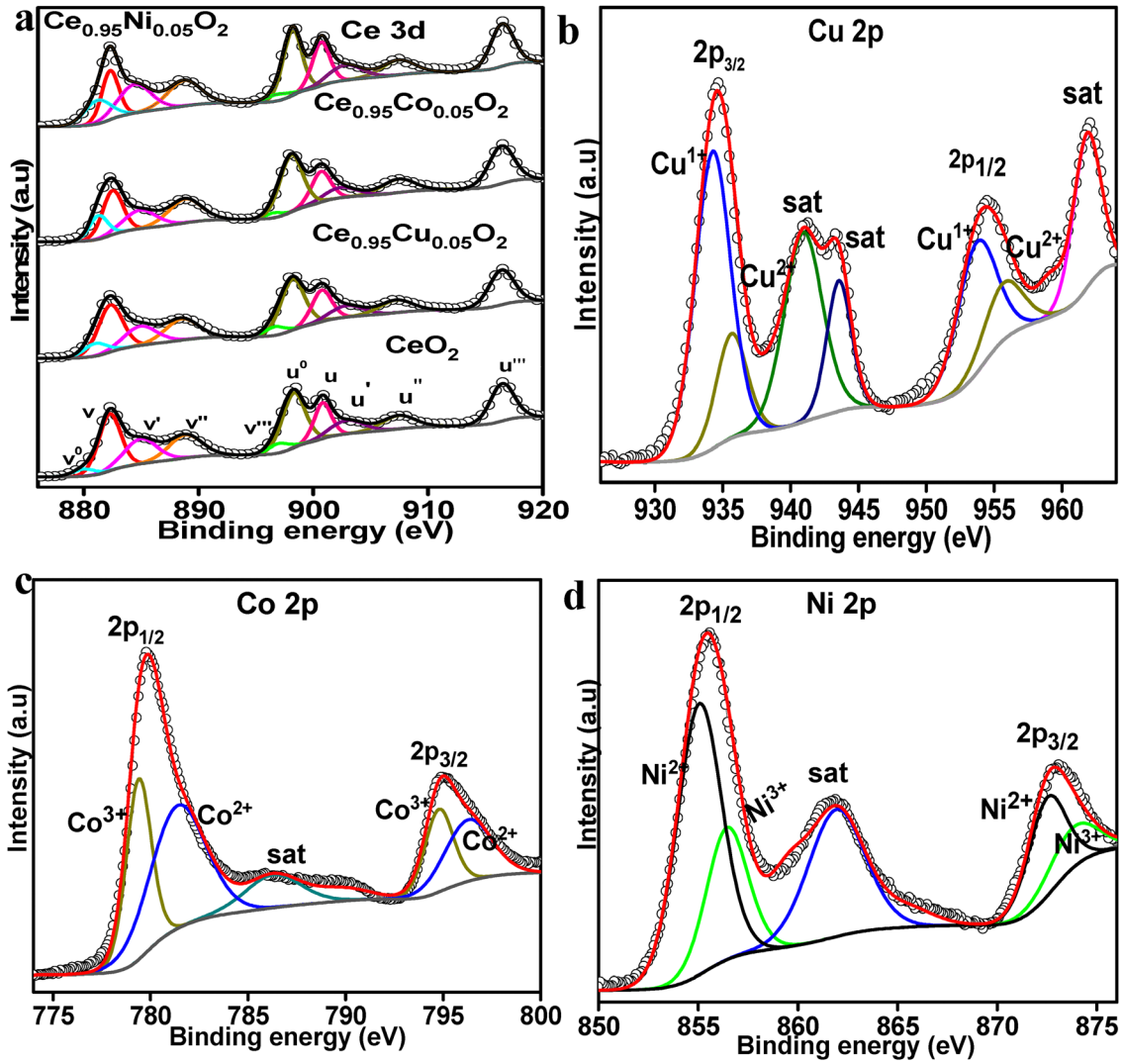

Fig. 9 (a) Ce 3d, (b) Cu 2p, (c) Co 2p and (d) Ni 2p core level spectra of the freshly synthesized pristine and doped solid solution oxides.

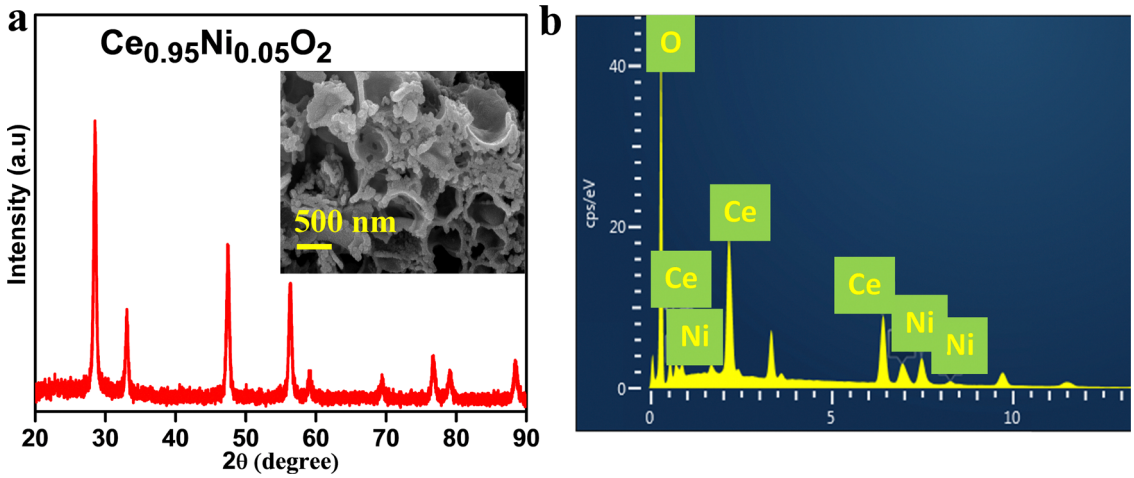

Fig. 10 (a) XRD and SEM image and (b) EDX of the exhausted $Ce_{0.95}Ni_{0.05}O_2$, catalyst.

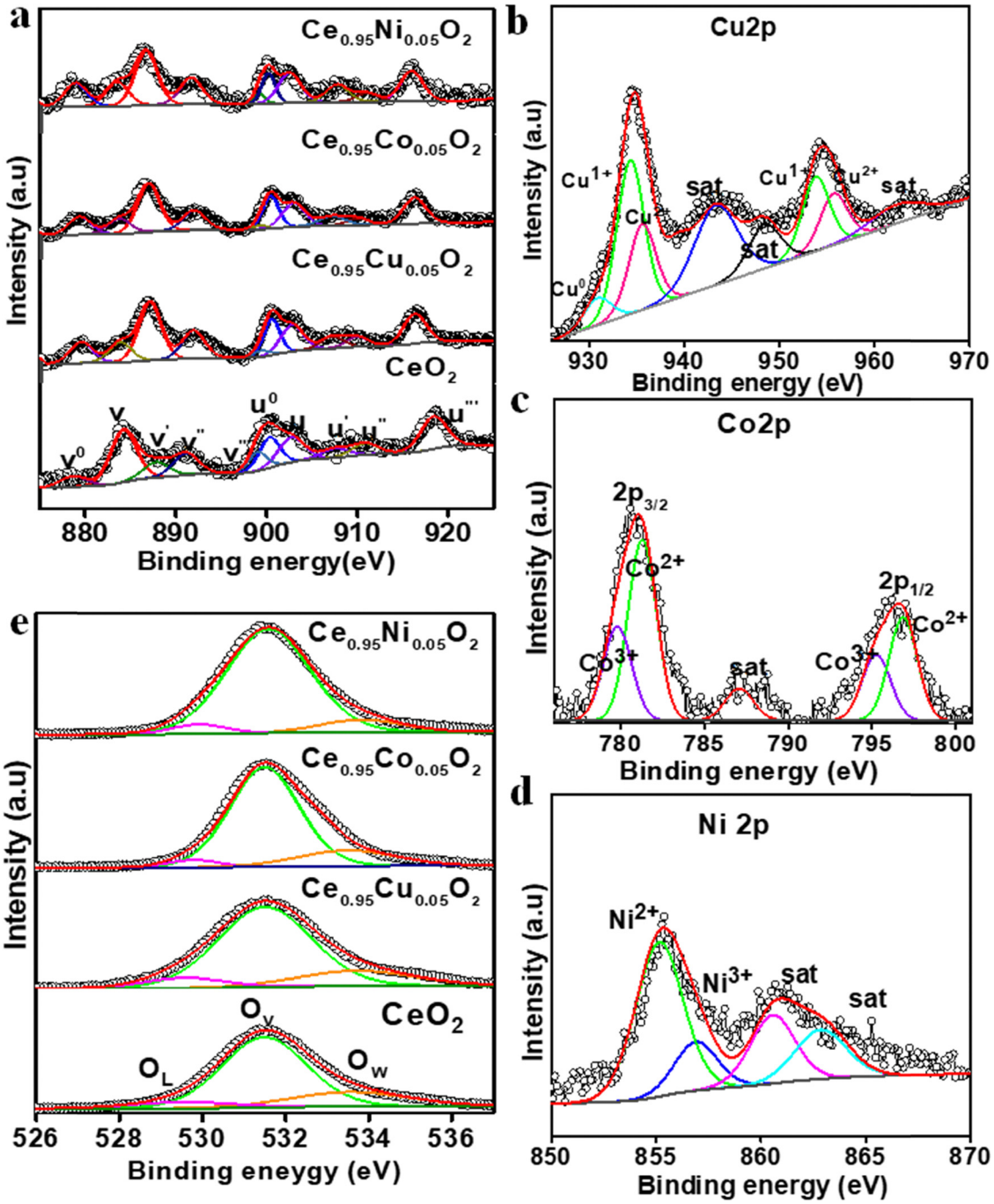

Fig. 11 (a) Ce 3d, (b) Cu 2p, (c) Co 2p, (d) Ni 2p and (e) O 1s core level spectra of the exhausted catalysts.

the Ni $2p_{3/2}$ peak corresponds to Ni^{2+} ions, indicating the maximum reduction of Ni during the HER process. Furthermore, we conducted the O 1*s* core level spectra of the exhausted catalysts (Fig. 11(e)). Interestingly, the vacancies increased significantly in the exhausted catalysts (vide O1s XPS of freshly prepared catalyst) after the HER, and the order of oxygen vacancies was in the following order: CeO_2 < $Ce_{0.95}Cu_{0.05}O_2$ < $Ce_{0.95}Co_{0.05}O_2$ < $Ce_{0.95}Ni_{0.05}O_2$. The substantial reduction of the formal oxidation states of Ni and Ce in $Ce_{0.95}Ni_{0.05}O_2$ compared to the other transition metals and support helped to create the highest oxygen vacancies in the material. The higher extent of reduction of Ni as well as Ce and the substantial presence of oxygen vacancies during the HER facilitated the H spill-over and consequently faster kinetics over $Ce_{0.95}Ni_{0.05}O_2$.

4. Conclusion

A one-step solution combustion approach was used to synthesize the pristine CeO_2 and doped $Ce_{0.95}Co_{0.05}O_2$, $Ce_{0.95}Ni_{0.05}O_2$,

and $Ce_{0.95}Cu_{0.05}O_2$ oxides. The production of phase-pure fluorite crystals with aliovalent ionic substitution of transition metals was validated by structural studies. The resulting porous nanocrystalline materials exhibited high oxygen vacancy concentrations, with $Ce_{0.95}Ni_{0.05}O_2$ demonstrating the highest values, as conclusively revealed through detailed spectroscopic analysis. Among the synthesized materials, $Ce_{0.95}Ni_{0.05}O_2$ displayed superior HER activity with enhanced kinetics. The HER overpotential (η_{10}) was measured at 139 mV, accompanied by an impressive mass activity of 95 mA mg^{-1} and remarkable stability over 24 hours. Detailed Tafel analysis identified the Volmer–Heyrovsky pathway as the operative HER mechanism for $Ce_{0.95}Ni_{0.05}O_2$. Further mechanistic investigations, including in-depth surface analysis, suggested a H spill-over phenomenon from the metal to the support, which facilitated faster HER kinetics in $Ce_{0.95}Ni_{0.05}O_2$.

Data availability

The data for this article are included herein.

Conflicts of interest

There are no conflicts to declare.

Acknowledgements

Authors thank Indian National Academy of Engineering (INAE) and Department of Science and Technology (DST), Government of India for the financial support (Project Sanction No. 2024/IN-TW/11).

References

1 A. P. van Troostwijk and J. R. Deiman, On a way to decompose Water into flammable Air & in vital air, *Obs. Phys.*, 1789, **35**, 369–384.
2 E. Gileadi, *Physical Electrochemistry: Fundamentals, Techniques and Applications*, Wiley-VCH Verlag, Weinheim, Germany, 2011.
3 R. W. Gurney, The quantum mechanics of electrolysis, *Proc. R. Soc. London, Ser. A*, 1931, **134**, 137–154.
4 B. E. Conway and J. O. Bockris, Electrolytic hydrogen evolution kinetics and its relation to the electronic and adsorptive properties of the metal, *J. Chem. Phys.*, 1957, **26**, 532–541.
5 J. K. Nørskov, T. Bligaard, A. Logadottir, J. R. Kitchin, J. G. Chen, S. Pandelov and U. Stimming, Trends in the exchange current for hydrogen evolution, *J. Electrochem. Soc.*, 2005, **152**, J23–J26.
6 B. Wei, J. Wu, G. Mei, Z. Qi, W. Hu and Z. Wang, $NiCo_2O_4$ Nanowire Arrays Rich in Oxygen Deficiencies for Hydrogen Evolution Reaction, *Int. J. Hydrogen Energy*, 2019, **44**, 6612–6617.
7 R. Manoharan and J. B. Goodenough, Hydrogen Evolution on $Sr_xNb_{3-\delta}$ ($0.7 \leq x \leq 0.95$) in Acid, *J. Electrochem. Soc.*, 1990, **137**, 910–913.
8 J. Chen, Z. Hu, Y. Ou, Q. Zhang, X. Qi, L. Gu and T. Liang, Interfacial Engineering Regulated by CeO to Boost Efficiently Alkaline Overall Water Splitting and Acidic Hydrogen Evolution Reaction, *J. Mater. Sci. Technol.*, 2022, **120**, 129–138.
9 W. Jin and J. Chen, Electrochemically Activated Cu_2O/Co_3O_4 Nanocomposites on Defective Carbon Nanotubes for the Hydrogen Evolution Reaction, *New J. Chem.*, 2018, **42**, 19400–19406.
10 J. Greeley, T. F. Jaramillo, J. Bonde, I. Chorkendorff and J. K. Nørskov, Computational High-Throughput Screening of Electrocatalytic Materials for Hydrogen Evolution, *Nat. Mater.*, 2006, **5**, 909–913.
11 C. T. Dinh, A. Jain, F. Arquer, P. D. Luna, J. Li, N. Wang, X. Zheng, J. Cai and B. Z. Gregory, *et al.*, Multi-Site Electrocatalysts for Hydrogen Evolution in Neutral Media by Destabilization of Water Molecules, *Nat. Energy.*, 2019, **4**, 107–114.
12 Z. Chen, G. Shao, Z. Ma, J. Song, G. Wang and W. Huang, Preparation of Ni–CeO_2 composite coatings with high catalytic activity for hydrogen evolution reaction, *Mater. Lett.*, 2015, **160**, 34–37.
13 A. Loiacono, S. Gutiérrez-Tarriño, V. Benavente Llorente, G. Lacconi, P. Oña-Burgos and E. A. Franceschini, Ni/Ru@NC-CeO_2 composite for hydrogen evolution reaction in alkaline media: Effect of CeO_2 decoration with Ru@NC on the catalytic activity, *J. Electroanal. Chem.*, 2023, **941**, 117548.
14 A. Macedo Andrade, Z. Liu, S. Grewal, A. J. Nelson, Z. Nasef, G. Diaz and M. H. Lee, MOF-derived Co/Cu-embedded N-doped carbon for trifunctional ORR/OER/HER catalysis in alkaline media, *Dalton Trans.*, 2021, **50**, 5473–5482.
15 K. P. CP, S. Aralekallu, V. K. Sajjan, M. Palanna, S. Kumar and L. K. Sannegowda, Non-precious cobalt phthalocyanine-embedded iron ore electrocatalysts for hydrogen evolution reactions, *Sustainable Energy Fuels*, 2021, **5**, 1448–1457.
16 S. Aralekallu, L. K. Sannegowda and V. Singh, Advanced bifunctional catalysts for energy production by electrolysis of earth-abundant water, *Fuel*, 2024, **357**, 129753.
17 S. Jing, J. Lu, G. Yu, S. Yin, L. Luo, Z. Zhang, Y. Ma, W. Chen and P. K. Shen, Carbon-Encapsulated WO_x Hybrids as Efficient Catalysts for Hydrogen Evolution, *Adv. Mater.*, 2018, **30**, 1705979.
18 S. Geng, Y. Q. Liu, Y. S. Yu, W. W. Yang and H. B. Li, Engineering Defects and Adjusting Electronic Structure on S-doped MoO_2 Nanosheets toward Highly Active Hydrogen Evolution Reaction, *Nano Res.*, 2020, **13**, 121–126.
19 K. K. Aruna and R. Manoharan, Electrochemical Hydrogen Evolution Catalysed by $SrMoO_4$ Spindle Particles in Acid Water, *Int. J. Hydrogen Energy.*, 2013, **38**, 12695–12703.
20 S. Roy, S. Payra, S. Challagulla, R. Arora, S. Roy and C. Chakraborty, Enhanced photoinduced electrocatalytic

oxidation of methanol using pt nanoparticle-decorated TiO_2–polyaniline ternary nanofibers, *ACS Omega*, 2018, **3**, 17778–17788.

21 T. Zheng, W. Sang, Z. He, Q. Wei, B. Chen, H. Li, C. Cao, R. Huang, X. Yan, B. Pan, S. Zhou and J. Zeng, Conductive tungsten oxide nanosheets for highly efficient hydrogen evolution, *Nano Lett.*, 2017, **17**, 7968–7973.

22 H. Tian, X. Cui, L. Zeng, L. Su, Y. Song and J. Shi, Oxygen vacancy-assisted hydrogen evolution reaction of the Pt/WO_3 electrocatalyst, *J. Mater. Chem. A*, 2019, **7**, 6285–6293.

23 P. C. Meenu, P. K. Samanta, T. Yoshida, N. J. English, S. P. Datta, S. A. Singh, S. Dinda, C. Chakraborty and S. Roy, Electro-oxidation reaction of methanol over $la_{2-x}Sr_xNiO_{4+\delta}$ ruddlesden–popper oxides, *ACS Appl. Energy Mater.*, 2022, **5**, 503–515.

24 D. Ghosh and D. Pradhan, Effect of cooperative redox property and oxygen vacancies on bifunctional OER and HER activities of solvothermally synthesized CeO_2/CuO composites, *Langmuir*, 2023, **39**, 3358–3370.

25 L. Zhang, X. Ren, X. Guo, Z. Liu, A. M. Asiri, B. Li, L. Chen and X. Sun, Efficient hydrogen evolution electrocatalysis at alkaline pH by interface engineering of Ni_2P–CeO_2, *Inorg. Chem.*, 2018, **57**, 548–552.

26 S. Swathi, R. Yuvakkumar, P. Senthil Kumar, G. Ravi, M. Thambidurai, C. Dang and D. Velauthapillai, Gadolinium doped CeO_2 for efficient oxygen and hydrogen evolution reaction, *Fuel*, 2022, **310**, 122319.

27 T. Li, J. Yin, D. Sun, M. Zhang, H. Pang, L. Xu, Y. Zhang, J. Yang, Y. Tang and J. Xue, Manipulation of Mott−Schottky Ni/CeO_2 heterojunctions into N-doped carbon nanofibers for high-efficiency electrochemical water splitting, *Small*, 2022, **18**, 2106592.

28 M. Zhao, Y. Li, H. Dong, L. Wang, Z. Chen, Y. Wang, Z. Li, M. Xia and G. Shao, The effects of CeO_2 nanorods and CeO_2 nanoflakes on Ni–S alloys in hydrogen evolution reactions in alkaline solutions, *Catalysts*, 2017, **7**, 197.

29 W. Liang, M. Zhou, X. Li, L. Zhu, Z. Li, Y. Zhou, J. Chen, F. Xie, H. F. Wang, N. Wang, Y. Jin and H. Meng, Oxygen-vacancy-rich MoO_2 supported nickel as electrocatalysts to promote alkaline hydrogen evolution and oxidation reactions, *Chem. Eng. J.*, 2023, **464**, 142671.

30 P. J. Sharma, N. A. Trivedi, K. S. Joseph, S. Siraj, P. Sahatiya, S. Dabhi, C. K. Sumesh and P. M. Pataniya, *Int. J. Hydrogen Energy*, 2024, **84**, 97–105.

31 H. Zhang, D. Shan, Y. Liu, L. Liu, G. Shen, S. Peng, D. Wang and X. Wang, Cerium-doped nickel phosphide nanosheet arrays as highly efficient electrocatalysts for the hydrogen evolution reaction in acidic and alkaline conditions, *ACS Appl. Energy Mater.*, 2022, **5**, 10961–10972.

32 S. Roy and S. Roy, Boosting water splitting via metal–support redox interaction in $Ce_{1-x}M_xO_{2-\delta}$ (M = Co, Ni, Cu), *ACS Appl. Nano Mater.*, 2024, **7**, 26534–26545.

33 P. C. Meenu and S. Roy, Unveiling the mechanistic significance of reducibility and lattice oxygen evolution in the $Ce_{1-x-y}Zr_xNi_yO_{2-\delta}$ catalyst for methanol electro-oxidation, *ACS Appl. Energy Mater.*, 2023, **6**, 11212–11225.

34 P. C. Meenu and S. Roy, Electro-oxidation reaction of methanol over reducible $Ce_{1-x-y}Ni_xSr_yO_{2-\delta}$: A mechanistic probe of participation of lattice oxygen, *ACS Appl. Mater. Interfaces*, 2023, **15**, 36154–36166.

35 S. Roy, A. Marimuthu, M. S. Hegde and G. Madras, High rates of NO and N_2O reduction by CO, CO and hydrocarbon oxidation by O_2 over nano crystalline $Ce_{0.98}Pd_{0.02}O_{2-\delta}$: Catalytic and kinetic studies, *Appl. Catal., B*, 2007, **71**, 23–31.

36 S. Roy, A. Marimuthu, M. S. Hegde and G. Madras, NO reduction by H_2 over nano-$Ce_{0.98}Pd_{0.02}O_{2-\delta}$, *Catal. Commun.*, 2008, **9**, 101–105.

37 S. Roy and M. S. Hegde, Pd ion substituted CeO_2: A superior de-NO catalyst to Pt or Rh metal ion doped ceria, *Catal. Commun.*, 2008, **9**, 811–815.

38 A. Gayen, T. Baidya, K. Biswas, S. Roy and M. S. Hegde, Synthesis, structure and three way catalytic activity of $Ce_{1-x}Pt_{x/2}Rh_{x/2}O_{2-\delta}$ (x = 0.01 and 0.02) nano-crystallites: Synergistic effect in bimetal ionic catalysts, *Appl. Catal., A*, 2006, **315**, 135–146.

39 J. Malleshappa, H. Nagabhushana, B. D. Prasad, S. C. Sharma, Y. S. Vidya and K. S. Anantharaju, Structural, photoluminescence and thermoluminescence properties of CeO_2 nanoparticles, *Optik*, 2016, **127**, 855–861.

40 S. Payra, S. K. Ganeshan, S. Challagulla and S. Roy, A correlation story of syntheses of ZnO and their influence on photocatalysis, *Adv. Powder Technol.*, 2020, **31**, 510–520.

41 T. Ye, W. Huang, L. Zeng, M. Li and J. Shi, CeO_{2-x} platelet from monometallic cerium layered double hydroxides and its photocatalytic reduction of CO_2, *Appl. Catal., B*, 2017, **210**, 141–148.

42 F. T. Li, Q. Wang, J. Ran, Y. J. Hao, X. J. Wang, D. Zhao and S. Z. Qiao, Ionic liquid self-combustion synthesis of BiOBr/$Bi_{24}O_{31}Br_{10}$heterojunctions with exceptional visible-light photocatalytic performances, *Nanoscale*, 2015, **7**, 1116–1126.

43 C. Zhang, D. Qin, Y. Zhou, F. Qin, H. Wang, W. Wang, Y. Yang and G. Zeng, Dual optimization approach to Mo single atom dispersed g-C_3N_4 photocatalyst: Morphology and defect evolution, *Appl. Catal., B*, 2022, **303**, 120904.

44 N. Mahmood, Y. Yao, J. W. Zhang, L. Pan, X. Zhang and J. J. Zou, Electrocatalysts for hydrogen evolution in alkaline electrolytes: Mechanisms, challenges, and prospective solutions, *Adv. Sci.*, 2018, **5**, 1700464.

45 E. B. Tetteh, M. Kim, A. Savan, A. Ludwig, T. D. Chung and W. Schuhmann, Reassessing the intrinsic hydrogen evolution reaction activity of platinum using scanning electrochemical cell microscopy, *Cell Rep. Phys. Sci.*, 2023, **4**, 101680.

46 H. K. Thakkar, K. K. Joshi, P. M. Pataniya, G. Bhadu, S. Siraj, P. Sahatiya and C. K. Sumesh, Photo-sensitive CuS/NiO heterostructure electrocatalysts for energy-saving hydrogen evolution reaction at all pH conditions, *Int. J. Hydrogen Energy*, 2023, **48**, 38266–38278.

47 B. Liu, Y. F. Zhao, H. Q. Peng, Z. Y. Zhang, C. K. Sit, M. F. Yuen, T. R. Zhang, C. S. Lee and W. J. Zhang, Nickel–cobalt diselenide 3D mesoporous nanosheet networks supported on Ni foam: An all-pH highly efficient integrated

electrocatalyst for hydrogen evolution, *Adv. Mater.*, 2017, **29**, 1606521.

48 G. Zhao, K. Rui, S. X. Dou and W. Sun, Heterostructures for electrochemical hydrogen evolution reaction: A review, *Adv. Funct. Mater.*, 2018, **28**, 1803291.

49 W. Karim, C. Spreafico, A. Kleibert, J. Gobrecht, J. Vande-Vondele, Y. Ekinci and J. A. van Bokhoven, Catalyst support effects on hydrogen spillover, *Nature*, 2017, **541**, 68–71.

50 S. Payra, S. Ray, R. Sharma, K. Tarafder, P. Mohanty and S. Roy, Photo- and electrocatalytic reduction of CO_2 over metal–organic frameworks and their derived oxides: A correlation of the reaction mechanism with the electronic structure, *Inorg. Chem.*, 2022, **61**, 2476–2489.

51 S. Payra and S. Roy, From trash to treasure: Probing cycloaddition and photocatalytic reduction of CO_2 over cerium-based metal–organic frameworks, *J. Phys. Chem. C*, 2021, **125**, 8497–8507.

52 S. Roy, P. Dahiya, T. K. Mandal and S. Roy, The role of reducibility *vis-à-vis* oxygen vacancies of doped Co_3O_4/CeO_2 in the oxygen evolution reaction, *Dalton Trans.*, 2024, **53**, 5484–5494.

53 S. Payra, N. Devaraj, K. Tarafder and S. Roy, Unprecedented Electroreduction of CO_2 over Metal Organic Framework-Derived Intermetallic Nano-Alloy $Cu_{0.85}Ni_{0.15}/C$, *ACS Appl. Energy Mater.*, 2022, **5**(4), 4945–4955.

54 P. K. R. Boppidi, P. Raj, S. Challagulla, S. R. Gollu, S. Roy, S. Banerjee and S. Kundu, Unveiling the dual role of chemically synthesized copper doped zinc oxide for resistive switching applications, *J. Appl. Phys.*, 2018, **124**, 214901.

55 S. Payra, S. Challagulla, R. R. Indukuru, C. Chakraborty, K. Tarafder and B. S. Roy, Ghosh The structural and surface modification of zeolitic imidazolate frameworks towards reduction of encapsulated CO_2, *New J. Chem.*, 2018, **42**, 19205–19213.

56 P. C. Meenu, S. Roy, C. Chakraborty and S. Roy, Electro catalytic oxidation reactions for harvesting alternative energy over non noble metal oxides: Are we a step closer to sustainable energy solution?, *Adv. Powder Technol.*, 2021, **32**, 2663–2689.

57 S. Y. Zhang, T. T. Li, H. L. Zhu and Y. Q. Zheng, Co_3O_4 polyhedrons with enhanced electric conductivity as efficient water oxidation electrocatalysts in alkaline medium, *J. Mater. Sci.*, 2018, **53**, 4323–4333.

58 S. Roy, N. Devaraj, K. Tarafder, C. Chakraborty and S. Roy, The role of synthesis *vis-à-vis* the oxygen vacancies of Co_3O_4 in the oxygen evolution reaction, *New J. Chem.*, 2022, **46**, 6539–6548.

59 S. Roy, T. Yoshida, A. Kumar, S. M. Yusuf, C. Chakraborty and S. Roy, Tailoring Co site reactivity via Sr and Ni doping in $LaCoO_3$ for enhanced water splitting performance, *Catal. Today*, 2024, **441**, 114885.

60 R. Gao, L. Pan, H. Wang, Y. Yao, X. Zhang, L. Wang and J. J. Zou, Breaking trade-off between selectivity and activity of nickel-based hydrogenation catalysts by tuning both steric effect and d-band center, *Adv. Sci.*, 2019, **6**, 1900054.

61 S. Roy and S. Roy, Activating cobalt inverse spinel oxides *via* Fe substitution for enhanced water splitting reaction, *Sustainable Energy Fuels*, 2024, **8**, 3854–3864.